

A NUMERICAL STUDY OF RELATIVISTIC BONDI-HOYLE ACCRETION ONTO A MOVING BLACK HOLE: AXISYMMETRIC COMPUTATIONS IN A SCHWARZSCHILD BACKGROUND

JOSÉ A. FONT^{1,2} AND J. M.^a. IBÁÑEZ²

Received 1997 June 30; accepted 1997 September 17

ABSTRACT

A fully relativistic numerical study of nonspherical Bondi-Hoyle accretion onto a Schwarzschild black hole is presented. The simulations are performed in axisymmetry with a high-resolution shock-capturing numerical scheme that makes use of a linearized Riemann solver as a key ingredient to handle shock waves. A broad family of initial flow parameters is considered. The main differences among the accretion patterns of the different models is discussed. A detailed comparative study with a previous relativistic simulation is performed. The results of this study reveal a qualitative agreement in the morphology and dynamics of the flow. However, there are important discrepancies concerning quantitative results as the mass accretion rates. All models evolved numerically in this paper relax to a final steady state accretion pattern, and, as the simulations are performed in axisymmetry, no evidence of any kind of instabilities (e.g., flip-flop) is present.

Subject headings: accretion, accretion disks — black hole physics — hydrodynamics — methods: numerical — relativity

1. INTRODUCTION

The canonical astrophysical scenario in which matter is accreted in a nonspherical way by a compact object is the one suggested originally by Bondi & Hoyle (1944). Using Newtonian gravity, they studied the accretion onto a gravitating point mass moving with constant velocity through a nonrelativistic gas that is at rest and has a uniform density at infinity. Since then, this pioneering analytic work has been numerically investigated, for a finite-size accretor, by a great number of authors over the years (see, e.g., Hunt 1971, 1979; Shima et al. 1985; Petrich et al. 1989; Matsuda, Inoue, & Sawada 1987; Matsuda et al. 1991, 1992; see also Ruffert & Arnett 1994 and Ruffert 1994a, 1994b, 1997, for an up-to-date reference list).

Apart from the Petrich et al. (1989, hereafter PSST) simulations, all authors employed Newtonian hydrodynamics assuming negligible relativistic effects. However, if the accretor is a black hole, a Newtonian treatment is inadequate. Newtonian hydrodynamics can be a valid approximation far from the hole, but it no longer holds when studying the flow evolution close to the inner boundary placed at the event horizon. Near that boundary, the problem is intrinsically relativistic or even ultrarelativistic both because of the velocities involved (approaching the speed of light) and because of the strong gravitational field. Fortunately, a simplifying assumption valid in many realistic situations is to neglect the self-gravity of the flow. By doing this, one is not forced to solve the Einstein field equations, and the problem reduces to study the dynamics of the flow in a fixed background gravitational field.

The almost total absence of simulations in the relativistic regime has to be found in the difficulties of an accurate numerical integration of the relativistic hydrodynamics system of equations in the extreme conditions of large

Lorentz factors and strong gravitational fields. The traditional approach of integrating the system with a finite-difference scheme with artificial viscosity fails at Lorentz factors typically greater than 2 (Norman & Winkler 1986). However, a better theoretical understanding of the hyperbolic character of the relativistic hydrodynamics system of equations (see Banyuls et al. 1997 and references therein) is to allow the use of modern numerical methods well developed in classical fluid dynamics. These schemes make use of exact or approximate Riemann solvers to capture discontinuities (shock waves) and are known as *high-resolution shock-capturing* schemes.

Focusing for now on pure Newtonian hydrodynamic Bondi-Hoyle accretion, let us start by reviewing the current status of the field. The results in the subsonic regime (asymptotic Mach number at infinity less than one) are in very good agreement among all authors. The flow patterns resemble those of spherical accretion with a global velocity component added. The matter flows toward the hole in a steady state manner, and after crossing the sonic point it free falls onto the hole.

However, this agreement is not so good in the supersonic regime, although a general standard picture has been emerging over the years. The discrepancies arise not only in the morphology of the flow in long-term simulations but also in some quantitative results such as the accretion rate estimates. This is related to the different numerical techniques employed and to the different ways of handling shock waves that appear only in the supersonic regime. Early low-resolution axisymmetric simulations found that the long-term flow pattern was in steady state (e.g., Shima et al. 1985; Anzer, Borner, & Monaghan 1987). These studies also found that the analytic Hoyle-Lyttleton accretion rate estimate (Hoyle & Lyttleton 1939),

$$\dot{M}_{\text{HL}} = \pi r_a^2 \rho_\infty v_\infty , \quad (1)$$

¹ Max-Planck-Institut für Gravitationsphysik Albert-Einstein-Institut Schlaatzweg 1, 14473 Potsdam, Germany.

² Departamento de Astronomía y Astrofísica Universidad de Valencia, 46100 Burjassot (Valencia), Spain.

was rather good despite its simplifying assumptions (a point-mass accretor and pressure effects neglected). In the above expression ρ_∞ and v_∞ are the asymptotic values of

the density and velocity of the medium, respectively, and r_a is the accretion radius, defined by

$$r_a = \frac{2GM}{v_\infty^2}, \quad (2)$$

where M is the mass of the accreting object and G is the gravitational constant. Later on, high-resolution two-dimensional nonaxisymmetric hydrodynamical computations in planar symmetry found that the flow did not approach a steady state in some cases (Matsuda et al. 1987; Fryxell & Taam 1988; Taam & Fryxell 1989). Instead, it exhibited a flip-flop behavior in which the shock cone oscillated from side to side accompanied by periods of disk formation. This kind of behavior not only appeared assuming ad hoc local density and velocity gradients in the vicinity of the accretor (Fryxell & Taam 1988; Taam & Fryxell 1989), which helps the development of unsteady flows, but also appeared in a natural way even considering accretion of uniform flows at infinity (Matsuda et al. 1991).

The first comparisons of two-dimensional and three-dimensional Newtonian computations were performed by Sawada et al. (1989). More recently, Ruffert & Arnett (1994) and Ruffert (1994a, 1994b, 1995, 1996) have extended the Bondi-Hoyle accretion problem to full three-dimensional numerical simulations using high-resolution methods and finer grids. In the case of supersonic accretion, important differences with previous work (notably, Matsuda et al. 1991, 1992; Taam, Fu, & Fryxell 1991) have been found. These mainly concern the stability of the *accretion cone* and the total absence of the flip-flop instability in the wake of the accretor. In Ruffert & Arnett (1994), results the flow remains stable, and there is only a slight deflection of the wake from side to side in the downwind direction. They found no flip-flop instability but only a turbulent wake.

The general picture that has emerged for Newtonian Bondi-Hoyle supersonic accretion has, as a key ingredient, a shock wave that can be attached or detached to the accreting object depending on the value of γ , the adiabatic exponent of the gas. For large values of γ ($4/3, 5/3$), the shock is placed mainly in the front part of the accretor, but as $\gamma \rightarrow 1$ (isothermal flow), the shock moves from the front part of the object ($5/3 \leq \gamma \leq 4/3$) and gets attached to its rear part (Ruffert 1996). Moreover, as the asymptotic Mach number of the flow increases, this shock cone resembles the cylindrical accretion column of Bondi & Hoyle (1944). Concerning the behavior of the wake, there is a correlation between its stability and the size of the accretor and the asymptotic Mach number for a fixed value of γ (Ruffert 1996; Benenohn, Lamb, & Taam 1997). As the size of the central object decreases and the Mach number increases, the wake is more turbulent and a steady state solution cannot be achieved. This morphological classification remains to be extended to the relativistic regime.

The extension of the nonspherical Bondi-Hoyle accretion to the Einsteinian theory of gravity was first achieved by PSST. These authors calculated the steady state accretion of matter onto a Schwarzschild black hole that is moving with a constant velocity through a uniform medium. Their simulations were axisymmetric, and they used standard finite-difference techniques with artificial viscosity. For their pioneering study, they considered a variety of flow velocities, sound speeds, and adiabatic indices, obtaining, for the first time, a broad picture for the wind accretion of material

moving near a black hole within a fully relativistic framework. Although their computations in the Newtonian limit reveal some qualitative agreement with previous numerical studies, especially for subsonic accretion, the discrepancies found in the supersonic regime are important. It is thus worthwhile to reinvestigate the problem to see if these uncertainties also propagate to the relativistic case.

On the other hand, in all Newtonian wind accretion computations performed over the years, it has been demonstrated that the original Bondi-Hoyle accretion picture, though qualitatively correct (and, in some cases quantitatively as well), was far too simple, especially for high Mach number flows. As computer power and resources were increasing, high-resolution nonaxisymmetric two-dimensional and mid-resolution three-dimensional computations started to reveal that the accretion process is highly nonsteady. This unsteady patterns were not obtained in unresolved earlier calculations, as Benenohn et al. (1997) have recently pointed out. In their Newtonian numerical studies, they have found that the problem is not fully resolved with fewer than 200 angular zones. The necessity of having an adequate angular resolution to account for the appearance of the wake instability has also implications on the amplitudes of the fluctuating accretion rates, which are smaller for large central objects (Ruffert 1994b). As mentioned previously, the general trend is that large objects and low Mach number flows may lead to steady state solutions, while smaller objects and higher Mach number flows may lead to a much more turbulent flow pattern. A low angular resolution could be valid in the former case but would be totally inadequate in the latter. It is extremely interesting to see how this extends to the relativistic case, which will be the scope of a subsequent paper. In this work we only look for steady state solutions, so the resolution employed is not so important. Let us also mention that PSST found always steady state solutions, but they used an extremely coarse grid of only 20 zones in the angular direction.

The aim of the present paper is to revisit some of the PSST computations and perform a detailed comparative study of the different accretion patterns that develop in the fully relativistic hydrodynamic accretion onto a moving black hole. In contrast to the PSST approach, this is done by using high-resolution shock-capturing schemes without artificial viscosity and making explicit use of the knowledge of the characteristic fields for the equations of general relativistic hydrodynamics. Let us mention that some preliminary results were presented in Banyuls et al. (1997).

The paper is organized as follows: in next section (§ 2) we present the system of equations of general relativistic hydrodynamics written as a hyperbolic system of conservation laws and describe the numerical procedure we use to solve them. The results of the simulations are presented and analyzed in § 3. Finally, § 4 summarizes the main conclusions of this work.

2. EQUATIONS AND NUMERICAL PROCEDURE

The equations describing the evolution of a relativistic fluid are *local conservation laws*: the local conservation of baryon number,

$$(\rho u^\mu)_{;\mu} = 0, \quad (3)$$

and the local conservation of energy-momentum,

$$(T^{\mu\nu})_{;\nu} = 0, \quad (4)$$

where ρ is the rest-mass density of the fluid, u^μ is its 4-velocity, and the subscript “;” stands for the covariant derivative. We choose units in which $G = c = 1$ and Greek (Latin) indices run from 0 to 3 (1 to 3). The stress-energy tensor is that of a perfect fluid, given by

$$T_{\mu\nu} = \rho h u_\mu u_\nu + p g_{\mu\nu}, \quad (5)$$

where h stands for the specific enthalpy, defined by $h = 1 + \epsilon + p/\rho$, with ϵ being the specific internal energy and p the pressure.

By choosing the appropriate set of variables, these equations can be explicitly written as a hyperbolic system of conservation laws. As described in Banyuls et al. (1997), this is done by defining quantities that are directly measured by Eulerian observers (York 1983), i.e., the rest-mass density (D), the momentum density in the j -direction (S_j), and the total energy density (E):

$$D = \rho W, \quad (6)$$

$$S_j = \rho h W^2 v_j, \quad (7)$$

$$E = \rho h W^2 - p. \quad (8)$$

Here, W stands for the Lorentz factor, which satisfies $W = (1 - v^2)^{-1/2}$ with $v^2 = \gamma_{ij} v^i v^j$, where v^i is the 3-velocity of the fluid, defined, for the case of a zero-shift vector, according to

$$v^i = \frac{u^i}{W}, \quad (9)$$

and γ_{ij} are the spatial components of the spacetime metric where the fluid evolves. We chose this metric to be the Schwarzschild one:

$$ds^2 = -\left(1 - \frac{2M}{r}\right)dt^2 + \left(1 - \frac{2M}{r}\right)^{-1} dr^2 + r^2(d\theta^2 + \sin^2 \theta d\phi^2) \quad (10)$$

where M is the mass of the hole.

With the above definitions, and expressed in Schwarzschild coordinates, the equations of general relativistic hydrodynamics can be written in a compact way as

$$\frac{1}{\sqrt{-g}} \left[\frac{\partial \sqrt{\gamma} U(\mathbf{w})}{\partial t} + \frac{\partial \sqrt{-g} \mathbf{F}^r(\mathbf{w})}{\partial r} + \frac{\partial \sqrt{-g} \mathbf{F}^\theta(\mathbf{w})}{\partial \theta} \right] = \mathbf{S}(\mathbf{w}), \quad (11)$$

where no ϕ derivatives appear as we are considering axisymmetry. In addition, $g \equiv \det(g_{\mu\nu})$ is such that

$$\sqrt{-g} = \alpha \sqrt{\gamma}, \quad \gamma \equiv \det(\gamma_{ij}),$$

where $\alpha = [1 - (2M/r)]^{1/2}$ and “det” stands for the determinant of the corresponding matrix.

In equation (11), the vector of primitive variables is

$$\mathbf{w} = (\rho, v_r, v_\theta, \epsilon), \quad (12)$$

and the vector of unknowns (conserved quantities) is

$$\mathbf{U}(\mathbf{w}) = (D, S_r, S_\theta, \tau). \quad (13)$$

The corresponding fluxes in the radial and azimuthal directions are, respectively,

$$\mathbf{F}^r(\mathbf{w}) = [Dv^r, S_r v^r + p, S_\theta v^r, (\tau + p)v^r], \quad (14)$$

$$\mathbf{F}^\theta(\mathbf{w}) = [Dv^\theta, S_r v^\theta, S_\theta v^\theta + p, (\tau + p)v^\theta], \quad (15)$$

and the corresponding vector of sources $\mathbf{S}(\mathbf{w})$ is

$$\begin{aligned} \mathbf{S}(\mathbf{w}) = & \left[0, -\frac{M}{\alpha^2 r^2} (S_r v^r + \tau + p + D) + \frac{1}{r} \right. \\ & \times (S_\theta v^\theta + 2p), p \cot \theta, -\frac{M}{\alpha^2 r^2} S^r \left. \right] \end{aligned} \quad (16)$$

In the above expressions, $\tau \equiv E - D$, the total energy density subtracting the rest-mass density.

We solve system (11) on a discrete numerical grid with a high-resolution shock-capturing numerical scheme that incorporates, as main ingredients, an approximate Riemann solver (Roe 1981) and a monotonic linear reconstruction of cell-centered quantities to cell interfaces (van Leer 1979). This code is the general-relativistic extension of the special-relativistic one described in Font et al. (1994).

The vector of conserved quantities, equation (13), is updated from level t^n to t^{n+1} according to the following algorithm:

$$\begin{aligned} \mathbf{U}_{i,j}^{n+1} = & \mathbf{U}_{i,j}^n - \frac{\Delta t}{\Delta V} [r_{i+1/2}^2 \hat{\mathbf{F}}_{i+1/2,j}^r - r_{i-1/2}^2 \hat{\mathbf{F}}_{i-1/2,j}^r] \\ & \times \Delta \cos \theta - \frac{\Delta t}{\Delta V} [\sin \theta_{j+1/2} \hat{\mathbf{F}}_{i,j+1/2}^\theta - \sin \theta_{j-1/2} \hat{\mathbf{F}}_{i,j-1/2}^\theta] \\ & \times \frac{\Delta r^3}{3} + \frac{\Delta t}{\Delta V} \frac{\Delta r^3}{3} \Delta \cos \theta S_{i,j} \end{aligned} \quad (17)$$

where $\Delta t = t^{n+1} - t^n$, $\Delta \cos \theta = \cos \theta_{j-1/2} - \cos \theta_{j+1/2}$, $\Delta r^3 = r_{i+1/2}^3 - r_{i-1/2}^3$ and indices i and j label the radial and angular zones, respectively. The volume element, ΔV is given by

$$\begin{aligned} \Delta V = & \int_{r_{i-1/2}}^{r_{i+1/2}} \int_{\theta_{j-1/2}}^{\theta_{j+1/2}} \sqrt{\gamma} dr d\theta = \Delta \cos \theta \left[\frac{1}{3} \alpha r^3 + \frac{5}{6} M \alpha r^2 \right. \\ & \left. + \frac{5}{2} M^2 \alpha r + \frac{5}{2} M^3 \log \frac{\alpha - 1}{\alpha + 1} \right]_{r_{i-1/2}}^{r_{i+1/2}}. \end{aligned} \quad (18)$$

In equation (17), $\mathbf{U}_{i,j}$ and $\mathbf{S}_{i,j}$ are the mean values of the state and source vector in the corresponding two-dimensional cell, while $\hat{\mathbf{F}}_{i+1/2,j}^r$ and $\hat{\mathbf{F}}_{i,j+1/2}^\theta$ are the numerical fluxes that have to be computed at the interfaces of neighbor numerical cells. These fluxes are calculated with an approximate Riemann solver, which uses the complete characteristic information contained in the Riemann problems between adjacent cells. It is based on the spectral decomposition of the Jacobian matrices of the general relativistic system of equations derived in Banyuls et al. (1997). The explicit expression is

$$\hat{\mathbf{F}}^i = \frac{1}{2} \left[\mathbf{F}^i(\mathbf{w}_R) + \mathbf{F}^i(\mathbf{w}_L) - \sum_{n=1}^4 |\tilde{\lambda}_n| \Delta \tilde{\omega}_n \tilde{\mathbf{r}}_n \right], \quad (19)$$

where \mathbf{w}_L and \mathbf{w}_R represent the values of the primitive variables at the left and right sides of a given cell interface and are obtained by means of a monotonic linear reconstruction of their cell-centered values (van Leer 1979). This procedure provides, in the absence of shocks, second-order accuracy in space. In equation (19), $\{\tilde{\lambda}_n, \tilde{\mathbf{r}}_n\}_{n=1,\dots,4}$ represent the eigenvalues and eigenvectors of the Jacobian matrices of system (11), and are evaluated at the cell-interface by using the

arithmetic mean of w_L and w_R . Quantities $\{\Delta\tilde{\omega}_n\}_{n=1,\dots,4}$, the jumps of the characteristic variables across each characteristic field, are obtained from

$$U(w_R) - U(w_L) = \sum_{n=1}^4 \Delta\tilde{\omega}_n \tilde{r}_n. \quad (20)$$

In order to gain accuracy in time, the code makes use of a third-order TVD (total variation diminishing) Runge-Kutta scheme (Shu & Osher 1988) to perform the time integration algorithm of equation (17), which is done simultaneously in both spatial directions. Finally, a one-dimensional Newton-Raphson iteration is used to compute in each time step the primitive variables from the conserved ones (see Martí & Müller 1996 for details). Tests of the code, both in one-dimensional and two-dimensional special and general relativistic hydrodynamics can be found in Font et al. (1994) and Banyuls et al. (1997). We refer the interested reader to these references for full details on the numerical code.

It maybe worthwhile to mention that, in its present version, the code is axisymmetric but employs the five hydrodynamics equations, i.e., it accounts for the ϕ -component of the velocity, too. Besides, it is explicitly written in terms of the Boyer-Lindquist coordinates for the Kerr spacetime metric, the reason being the possibility of computing the ϕ -component of the proper velocity when dealing with the Kerr metric. The results presented here are for zero Kerr angular momentum parameter.

3. SIMULATIONS

All simulations presented in this paper are in axisymmetry. With this configuration we can study flows evolving in the background field of nonrotating holes, as well as that of rotating holes whose motion throughout the external medium is aligned with the direction of the rotation axis. We only consider here nonrotating holes. Results for Kerr black holes will be reported in a future paper. We will also extend this analysis to more general nonaxisymmetric configurations.

3.1. Initial Setup

To completely specify the flow it is only necessary to consider the following set of asymptotic initial parameters: v_∞ , which is the hole/medium relative velocity, c_{s_∞} , which is the sound speed of the ambient gas, and γ , which is the constant adiabatic index of the medium. The first two parameters fix the asymptotic Mach number, M_∞ . The external medium obeys a perfect fluid equation of state:

$$p = (\gamma - 1)\rho\epsilon. \quad (21)$$

The covariant components of the initial velocity are given in terms of its asymptotic value:

$$v_r = \frac{1}{\sqrt{\gamma^{rr}}} v_\infty \cos \theta, \quad (22)$$

$$v_\theta = -\frac{1}{\sqrt{\gamma^{\theta\theta}}} v_\infty \sin \theta. \quad (23)$$

Initially, the whole grid is filled with these asymptotic initial values. We let the flow evolve toward a steady state accretion pattern.

The spatial numerical domain, (r, θ) , is covered by 200×40 numerical cells. The radial and angular discretizations lie, respectively, in the interval $r_{\min} \leq r \leq r_{\max}$ and $0 \leq \theta \leq \pi$, where r_{\min} and r_{\max} depend on the particular model (see below). For the angular direction we have used an equally spaced grid, while in the radial direction we have employed the Schwarzschild tortoise coordinate defined by $r_* = r + 2M \ln [(r/2M) - 1]$. This permits a high resolution at the innermost radial zones where the hydrodynamical variables show their more extreme values. We are using a finer resolution, in both r and θ directions, than PSST, who show results only with a very coarse grid of 40 radial and 20 angular zones. It is interesting to mention that in spite of that poor resolution, they are able to simulate flows evolving in a ultrarelativistic regime (from the thermodynamical point of view). For comparison purposes we have also run some of our models with this coarser grid.

We have checked the convergence properties of our numerical solution by running some of the models with four different angular resolutions, namely, 20, 40, 80, and 160 zones. We have found that the choice of 40 angular zones suffices to find a converged solution, and, in consequence, all models have been computed with this canonical angular resolution. It is worth mentioning that the possibility of using such a low angular resolution is motivated by the fact that we are considering axisymmetric flows that evolve toward a final steady state regime.

As mentioned at the introduction, the natural length scale in this astrophysical scenario is the accretion radius given by equation (2). For comparison purposes, we employ the same definition as PSST, namely,

$$r_a = \frac{M}{(v_\infty^2 + c_{s_\infty}^2)}. \quad (24)$$

Except by a factor of 2, both expressions are equivalent in the Newtonian regime, where $c_{s_\infty} \rightarrow 0$. The position of the inner and outer zones for the different models in units of the accretion radius is listed in Table 1.

The boundary conditions in the radial direction are as follow: we impose outflow boundary conditions at the interior. This is the right condition considering that the matter will always flow supersonically onto the hole at that distance. In practice, we just copy the values of all quantities, except the radial velocity, in the first zone to the boundary zones. For the radial velocity we perform a linear extrapolation. In the outer radius we distinguish being in the upwind or downwind hemispheres. In the latter case we impose outflow boundary conditions as all gradients should vanish. On the contrary, in the upwind hemisphere, we always consider the initial asymptotic values of all variables at r_{\max} . In the angular direction, as we are using an axisymmetric code, reflecting boundary conditions are chosen at the poles ($\theta = 0, \pi$).

The set of models that has been considered is listed in Table 1. These models are equivalent to some of the ones considered by PSST. The first six models in Table 1 correspond to *mildly relativistic* models. They are mildly relativistic from the thermodynamical point of view. All of them have an asymptotic sound speed $c_{s_\infty} = 0.1$. However, they are not so from the kinematical point of view, because, as the evolution proceeds, the infalling velocity at the innermost zones can reach values very close to one. In addition, the last five models in Table 1 correspond to *ultrarelativistic*

TABLE 1
INITIAL MODELS

| Model | c_{s_∞} | γ | \mathcal{M}_∞ | v_∞ | $r_a(M)$ | $r_{\min}(r_a)$ | $r_{\max}(r_a)$ | $t_f(M)$ |
|----------|----------------|----------|----------------------|------------|----------|-----------------|-----------------|----------|
| MA1..... | 0.1 | 1.1 | 1.5 | 0.15 | 30.8 | 0.125 | 10.0 | 4000 |
| MA2..... | 0.1 | 1.1 | 5.0 | 0.5 | 3.8 | 0.57 | 10.0 | 750 |
| MB1..... | 0.1 | 4/3 | 1.5 | 0.15 | 30.8 | 0.125 | 10.0 | 4000 |
| MB2..... | 0.1 | 4/3 | 5.0 | 0.5 | 3.8 | 0.57 | 10.0 | 750 |
| MC1..... | 0.1 | 5/3 | 1.5 | 0.15 | 30.8 | 0.125 | 10.0 | 2000 |
| MC2..... | 0.1 | 5/3 | 5.0 | 0.5 | 3.8 | 0.44 | 10.0 | 750 |
| UA1..... | 0.31 | 1.1 | 1.5 | 0.47 | 3.2 | 0.69 | 9.38 | 200 |
| UA2..... | 0.31 | 1.1 | 3.0 | 0.93 | 1.04 | 2.12 | 28.85 | 110 |
| UB0..... | 0.57 | 4/3 | 0.6 | 0.34 | 2.2 | 1.0 | 13.64 | 200 |
| UB1..... | 0.57 | 4/3 | 1.5 | 0.86 | 0.92 | 2.39 | 32.61 | 200 |
| UC0..... | 0.81 | 5/3 | 0.6 | 0.49 | 1.1 | 2.0 | 27.27 | 200 |

NOTE.— c_{s_∞} is the asymptotic sound speed, γ is the adiabatic exponent, \mathcal{M}_∞ is the asymptotic Mach number, v_∞ is the asymptotic flow velocity, r_a is the accretion radius, r_{\min} and r_{\max} are the minimum and maximum radial values of the computational domain, and t_f is the final time at which the simulation is stopped.

models, where the asymptotic value of the sound speed is equal to its maximum permitted value,

$$c_{s_{\max}} = \sqrt{\gamma - 1}. \quad (25)$$

Let us point out that in our set of ultrarelativistic initial models there are two *extreme* cases that were not previously evolved by PSST. These are models UA2 and UB1, for

which the sound speed is very close to its maximum permitted value and the asymptotic flow velocity is close to c .

3.2. Mildly Relativistic Models

In Figures 1 and 2 we show the transition to steady state for model MB1. This model has an asymptotic velocity $v_\infty = 0.15$ and Mach number $\mathcal{M}_\infty = 1.5$. The adiabatic

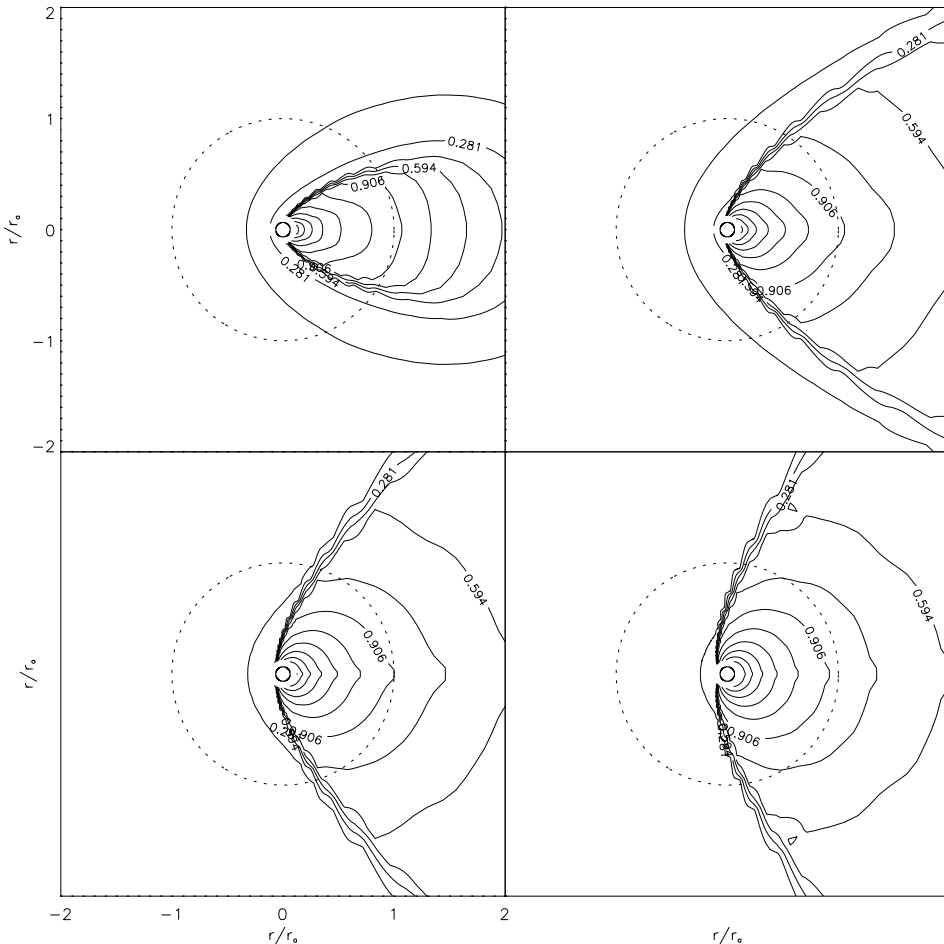


FIG. 1.—Evolution of the logarithm of the density normalized to the asymptotic value for model MB1. From top left to bottom right the corresponding time, in units of M , is 400, 1000, 2000, and 4000. Last snapshot corresponds to the steady state. The dotted-line circle represents the accretion radius.

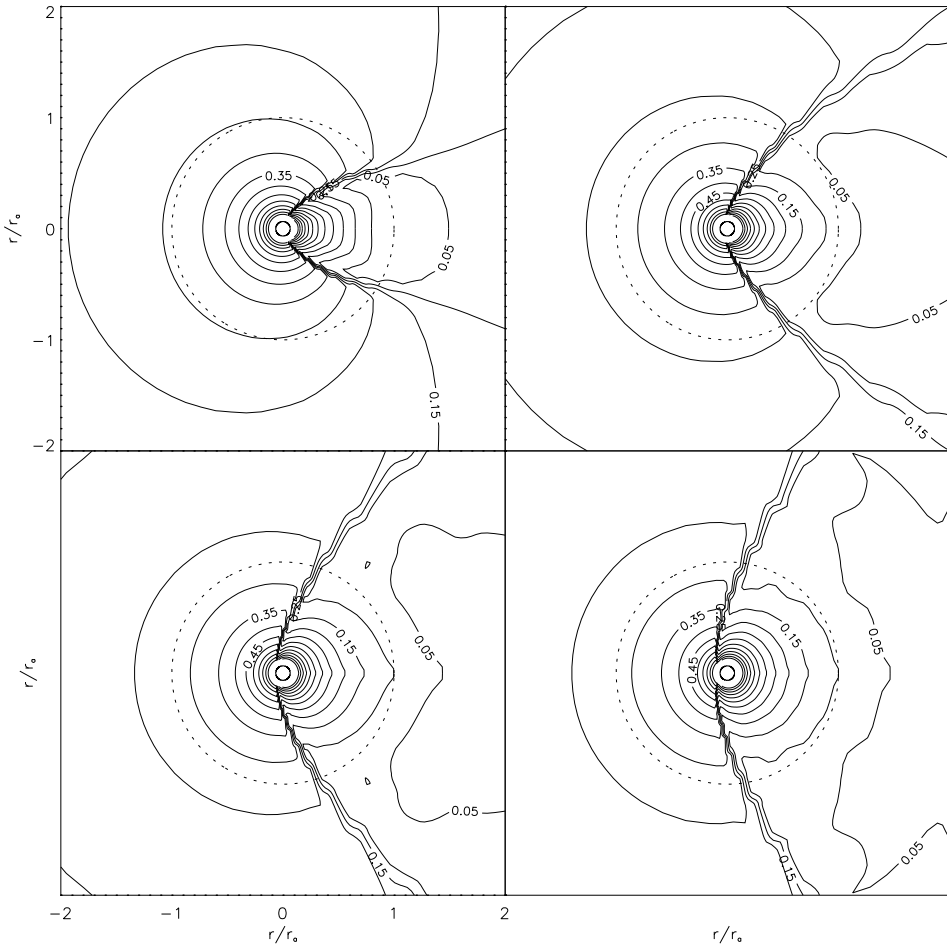


FIG. 2.—Evolution of the total velocity normalized to the asymptotic value for model MB1. From top left to bottom right the corresponding time, in units of M , is 400, 1000, 2000, and 4000. Last snapshot corresponds to the steady state. The dotted-line circle represents the accretion radius.

exponent is $\gamma = 1.1$. We plot only an evolutionary sequence for this model. For the remaining models we show only a snapshot of their evolution once steady state, if any, has been reached. To describe the morphology and dynamics of the flow, we chose to represent isocontours of the logarithm of the density and velocity. Both variables are always normalized to the corresponding asymptotic values.

Soon after the evolution starts, the material is focused on the rear part of the hole by the gravitational attraction of the hole. For a pressureless gas, the density at this symmetry line could reach an infinite value and matter would flow onto the hole along this accretion line. However, as internal energy and pressure increase, a cylindrical shock forms around this line. The high-density postshock region resembles the accretion column theoretically predicted by Bondi & Hoyle (1944). This can be clearly seen from the evolutionary sequence of Figures 1 and 2. As the evolution proceeds, this cylindrical shock rapidly gets disturbed and begins to open to increasingly wide angles. At this part of the evolution, the flow of material toward the hole occurs mainly inside the accretion cone. The solution relaxes to a steady state accretion pattern, where the accretion cone remains fixed and stable. The part of the shock closer to the inner radius moves, during the evolution, from the rear part of the hole toward its front, accommodating finally at an angular position slightly bigger than $\pi/2$ (Figs. 1 and 2,

bottom left, $t = 2000M$; bottom right, $t = 4000M$). The final position of the shock depends on the specific values of γ and \mathcal{M}_∞ : models with large values of γ ($\geq 5/3$) and moderate Mach numbers present a detached shock wave in front of the accretor (see model MC1 below), in agreement with classical simulations.

On the other hand, far from the hole, the transition to steady state occurs much more slowly. Here, the changes happen in a timescale on the order of r_{\max}/v_∞ , which for this model is roughly $2000M$. This makes these computations very CPU time consuming. A good way to see if the simulation relaxes to a steady state is to analyze the mass accretion rate at different radii from the hole (see § 3.4 below for definitions). For model MB1, a time evolution of the integrated mass accretion rate as a function of the radial coordinate is presented in Figure 3. As can be clearly seen from this plot, the transition to steady state in the interior zones happens faster than in the exterior. At the final time of the evolution of this model ($t = 4000M$), the radial profile is *almost* constant, indicating that the solution is close enough to the steady state in the whole grid. This is the best indicator to see if the final solution is stationary as, in the absence of sources and sinks in the domain, the mass accretion rate has to be independent of the radial distance at which is computed. The high Mach number mildly relativistic models (MA2, MB2, and MC2) and the whole subset of

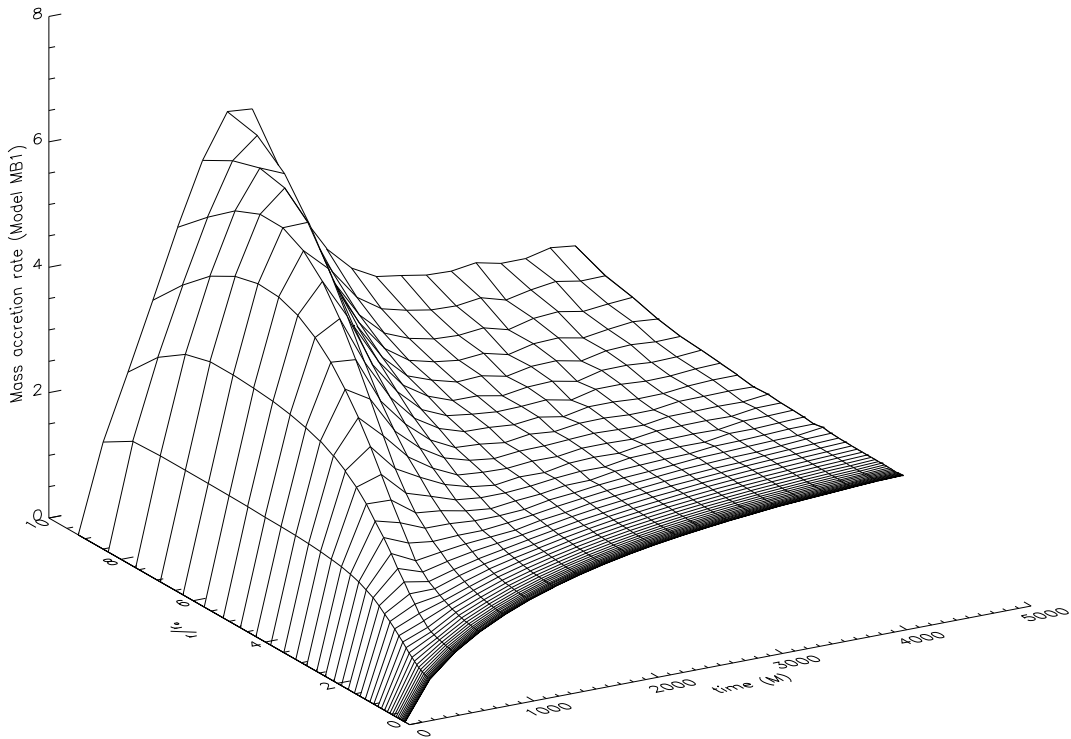


FIG. 3.—Time evolution of the mass accretion rate at different radii from the hole for model MB1. Note how long it takes to the exterior to reach a flat profile.

ultrarelativistic models show more clearly constant accretion rate values in the whole domain at earlier times than models MA1, MB1, and MC1.

We have run model MB1 with four different angular resolutions in order to check the convergence properties of the code, as well as the possible appearance of instabilities in the shock cone. We found that the overall morphology was completely similar with 20, 40, 80, and 160 angular zones. The shock was placed exactly at the same location by the end of the simulation ($t = 4000M$), and the same happened to the stagnation point at the rear part of the hole. In addition, the computed mass accretion rates (§ 3.4) showed not only identical values at the last snapshot but also the same transition profile toward steady state. Figure 4 shows the logarithm of the rest-mass density for the four different angular resolutions at the final time of the evolution of model MB1. Notice that the coarser angular grid has the same resolution as PSST computations.

Figures 5–9 show isocontours of the logarithm of the density and velocity for the rest of mildly relativistic models. The top panels of these figures always show a closer view of the innermost region, and the contours appear labeled and normalized to their initial asymptotic values. In addition, the bottom panels show the complete numerical domain. Let us draw your attention to the fact that scales are different in both sets of panels. One can see that the shock wave clearly extends from the surroundings of the hole all the way up to the outer boundary. We point out that although an expected amount of diffusion appears at large distances, the shock can be easily tracked up to this region. We also point out the goodness of our outer boundary condition, which shows no signs of being affecting the final solution. This is particularly true for most of the models, as they have

a supersonic asymptotic Mach number. It is worth indicating, however, that for subsonic flows at infinity, as is the case of the ultrarelativistic models UB0 and UC0 (see below), this boundary condition could be affecting somehow the results, as information could eventually propagate back upstream the outer zones. We have not investigated this issue in the present paper.

Qualitatively, these figures show the same morphological features as their PSST counterparts. They are also identical to what has been previously found in supersonic Newtonian simulations (see, e.g., Ruffert 1994b, 1995, 1996, and references therein). All mildly relativistic models considered here have a supersonic asymptotic Mach number, and, hence, a shock wave and an accretion cone are always present. Despite this general morphological agreement, important differences concerning the stability and position of the shock, as well as the mass accretion rates, appear. Figures 4–8 can be directly compared with the ones presented by PSST. Unfortunately, in PSST work, there is no indication of the exact time at which the simulation is stopped, making a direct comparison impossible. Hence, we will assume that, in all cases, their solution has relaxed to the steady state.

The main conclusion that emerges from these figures is that all models show a remarkable stable accretion cone. This is especially true for low Mach number models. For high Mach number models, the shock moves slightly around a central equilibrium position. We have checked this by performing an animation of the different snapshots every $50M$ up to $750M$ for models MB2 and MC2. Once the shock settles down to its equilibrium value, we can notice some perturbations traveling along the shock up to short radial distances, the outermost parts being totally unaffected by this process. In addition, there is also, in the

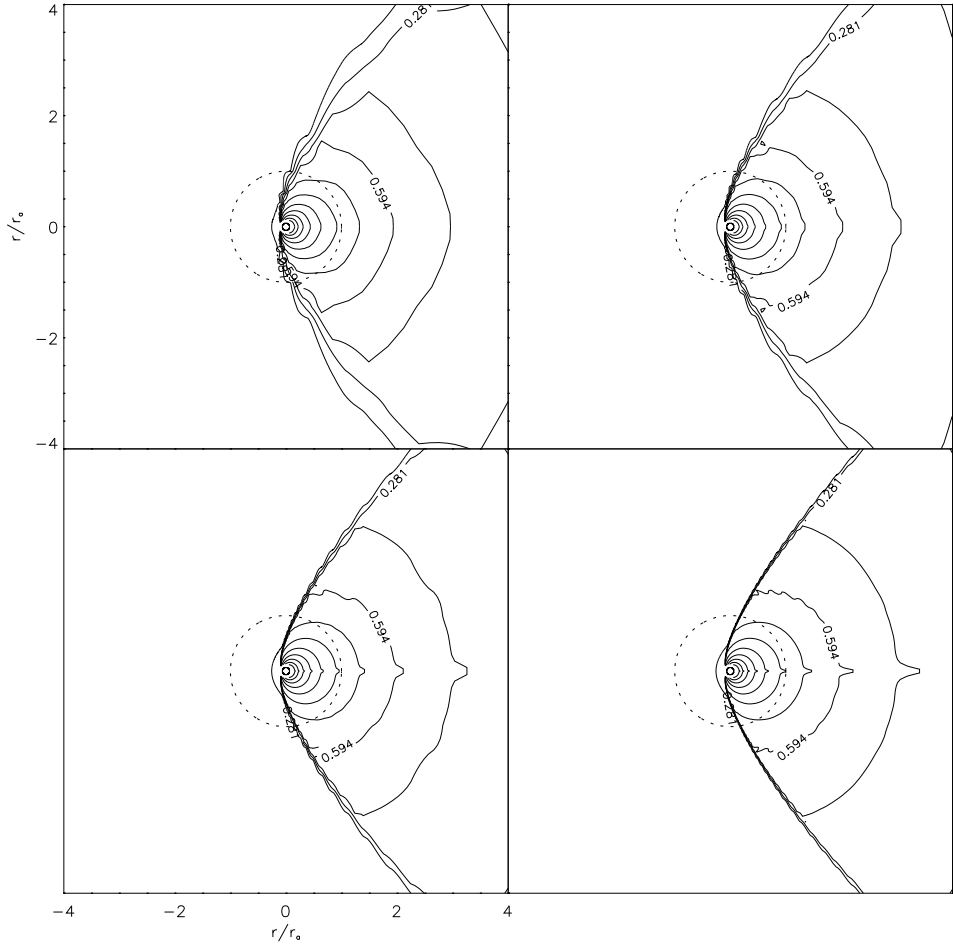


FIG. 4.—Isocontours of the logarithm of the rest-mass density for model MB1 with four different number of angular zones: 20 (top left), 40 (top right), 80 (bottom left), and 160 (bottom right). Note that the morphology is identical in the four cases, indicating that a resolution of only 20 angular zones is enough to display all features. Obviously, the shock appears less diffuse as the resolution increases. The top left-hand panel corresponds to the same angular resolution as PSST computations.

high-resolution runs, a small indication of vortex shedding in the rear part of the hole, which could give rise to a turbulent wake. More resolution maybe needed to properly account for this vortex emission. We have also found that the equilibrium position of the shock cone does not depend on the angular resolution we employ. The small fluctuations of the shock cone, especially in model MB2, cause the computed accretion rate to oscillate around a central value, as can be seen in Figure 17b below. The amplitude of the oscillations is again independent of the angular resolution. We do not find any sign of flip-flop instability, in complete agreement with all previous works—Newtonian and relativistic—that considered axisymmetric configurations (Hunt 1971, 1979; Shima et al. 1985; PSST). As mentioned at the introduction, this kind of behavior has appeared *only* in two-dimensional *nonaxisymmetric* classical calculations (Matsuda et al. 1987; Fryxell & Taam 1988; Taam & Fryxell 1989; Benensohn et al. 1997). It is worth pointing out again the total absence for this kind of instability in three-dimensional classical simulations (Ruffert & Arnett 1994). In three-dimensions, this instability only appears assuming initial transverse velocity gradients (Ruffert 1997).

A direct inspection of Figures 5–9 show that the shock cone is closer to the rear part of the hole for large Mach

number models (MA2, MB2, and MC2; all $\mathcal{M}_\infty = 5$). Figures 5–9 also reveal that this position greatly depends on the adiabatic index γ . For $\gamma \leq 4/3$ we do not find detached shocks for the specific values of \mathcal{M}_∞ that we have considered. Model MB1 is almost on the limit: the shock is attached to the hole but almost succeeds in cleaning its whole surface. For $\gamma = 5/3$ the shock is detached, but only for model MC1 with $\mathcal{M}_\infty = 1.5$. This morphological trend also applies to classical computations (e.g., Ruffert & Arnett 1994; Ruffert 1994a, 1994b, 1995, 1996) and was also found by PSST, although some discrepancies arise again. These mainly concern the angle of the shock with the symmetry axis (see below). Moreover, the stand-off position of the detached shock in model MC1 is quite different: we find that the shock is placed at $r \approx 0.5r_a$, while PSST found $r \approx 3 - 4r_a$. We have also noticed that the position of the detached shock does not depend on the resolution we employ. With their coarser grid of 40 radial zones and 20 angular zones, we obtain that the shock is located at roughly the same distance. As expected, the scaled mass accretion rate with both different resolutions is very similar. On the other hand, model MC2 also shows an important difference in the position of the attached tail shock in the surface of the hole, as can be seen comparing Figure 9 with

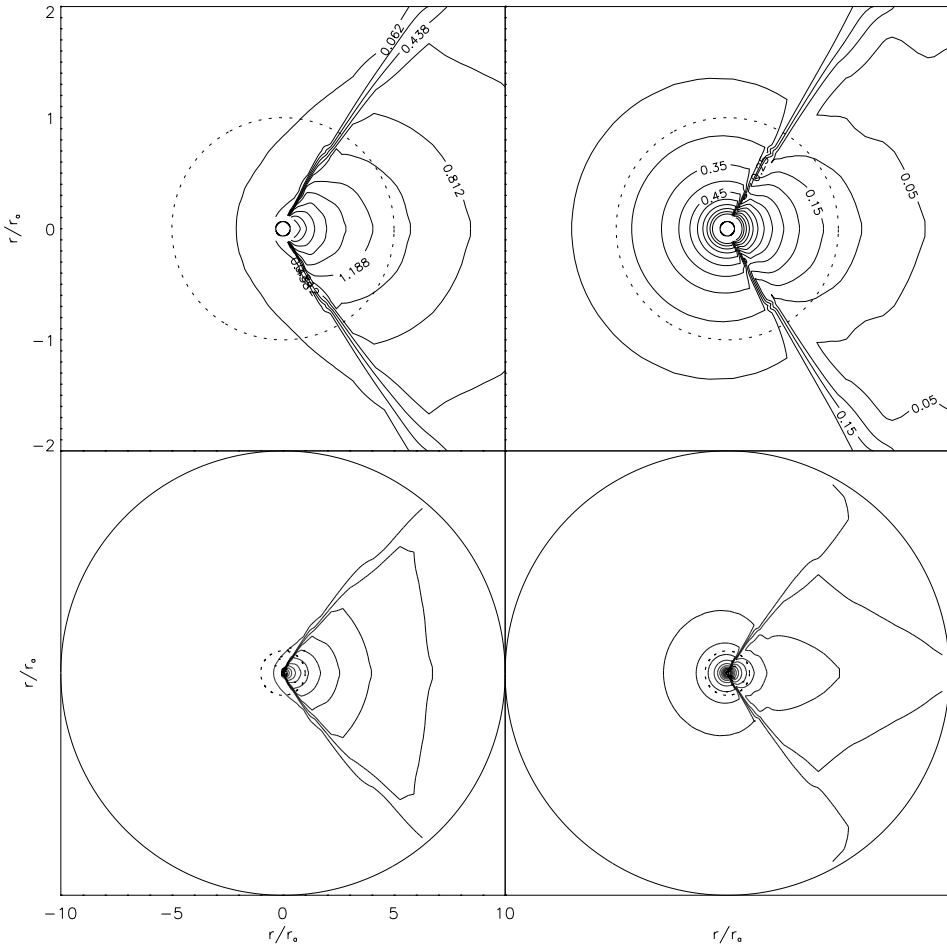


FIG. 5.—*Top:* Close-up view of the logarithm of density (*left*) and velocity for model MA1 at $t = 4000M$. *Bottom:* Full computational domain view. Note that despite a small amount of diffusion the shock can be clearly followed up to the outer boundary, which is defined by the outer solid circle. The dashed circle represents the accretion radius.

Figures 17 and 18 of PSST.

All models present a point of zero velocity at the axis on the downwind direction, the so-called stagnation point. The position of this point, r_{sp} , determines the accretion rates of mass and momentum: all material inside r_{sp} is ultimately

captured by the hole, while material outside r_{sp} escapes away. We have summarized the position of the stagnation point for the different models in Table 2, where we also write, whenever possible, the values by PSST for comparison. A time evolution of r_{sp} for the mildly relativistic models

TABLE 2
SUMMARY OF RESULTS

| Model | θ_a | θ_c | θ_{PSST} | \bar{r}_{sp} | r_{sp}^{PSST} | v_{\max}^u | v_{\max}^d | \mathcal{M}_{\max}^u | \mathcal{M}_{\max}^d |
|----------|------------|------------|-----------------|----------------|-----------------|--------------|--------------|------------------------|------------------------|
| MA1..... | 41.8 | 44 | 75 | 2.37 | ... | 0.72 | 0.67 | 7.04 | 5.28 |
| MB1..... | 41.8 | 42 | 75 | 2.19 | ... | 0.72 | 0.65 | 6.66 | 3.22 |
| MC1..... | 41.8 | 38 | 80 | 1.50 | > 3 | 0.48 | 0.60 | 1.20 | 1.84 |
| MA2..... | 11.5 | 22 | 30 | 7.29 | 1.7 | 0.96 | 0.94 | 9.89 | 5.67 |
| MB2..... | 11.5 | 21 | 22.5 | 5.46 | ... | 0.96 | 0.93 | 10.92 | 2.93 |
| MC2..... | 11.5 | 27 | 35 | 3.42 | 1.9 | 0.96 | 0.90 | 14.52 | 1.79 |
| UA1..... | 41.8 | 47 | 95 | 3.24 | ... | 0.96 | 0.91 | 3.10 | 2.93 |
| UA2..... | 19.5 | 15 | ... | 7.35 | ... | 0.99 | 0.91 | 3.29 | 2.89 |
| UB0..... | ... | ... | ... | 2.70 | ... | 0.91 | 0.86 | 1.59 | 1.51 |
| UB1..... | 41.8 | 35 | ... | 5.22 | ... | 0.99 | 0.85 | 1.74 | 1.48 |
| UC0..... | ... | ... | ... | 3.88 | ... | 0.89 | 0.81 | 1.10 | 1.00 |

NOTE.— θ_a is the analytical value for the shock opening angle at large distances according to $\sin^{-1} 1/\mathcal{M}_\infty$, θ_c is our numerical result, θ_{PSST} is the result by PSST, \bar{r}_{sp} is the mean value of the stagnation point position, r_{sp}^{PSST} is the value by PSST, v_{\max}^u is the maximum value of the velocity in the upwind direction along the line $\theta = \pi$, v_{\max}^d is the maximum velocity value in the downwind direction ($\theta = 0$), \mathcal{M}_{\max}^u is the maximum value of the upwind Mach number, and \mathcal{M}_{\max}^d is its corresponding maximum value in the downwind direction.

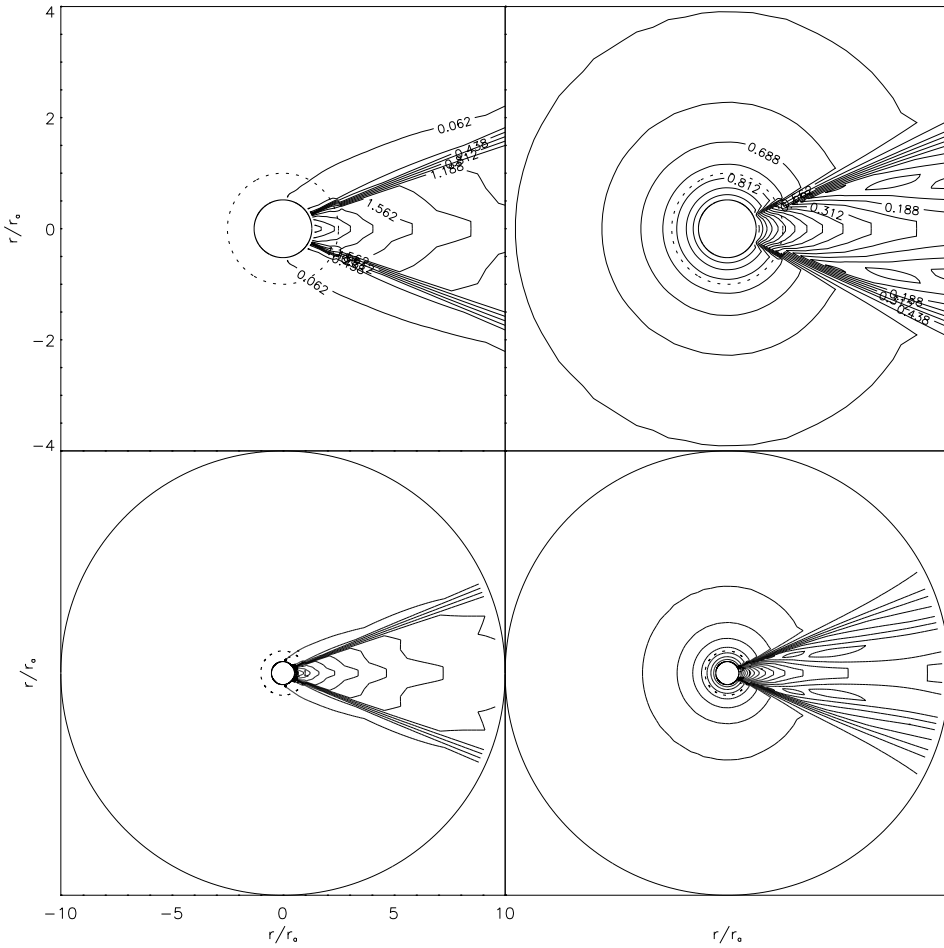


FIG. 6.—*Top:* Close-up view of the logarithm of density (left) and velocity for model MA2 at $t = 750M$, once the steady state has been reached. *Bottom:* Full computational domain view.

appear in Figures 16a and 16b below. Note that the low Mach number models show more stable positions of the stagnation point, while high Mach number models reveal more abrupt changes. However, the history of the stagnation point position becomes much more smooth when the resolution is increased, the final value being, in general terms, independent of the resolution. It is worthwhile to point out the large discrepancies found with PSST results, at least for the three models where the comparison is possible (MA2, MC1, and MC2). As one could expect, for larger values of v_∞ , we get larger values of r_{sp} . They seem to get the opposite trend. This disagreement could explain the discrepancies found in the computed mass accretion rates (see below).

We have also compared the shock opening angle with the value predicted analytically for large distances from the object, $\theta_a = \sin^{-1}(1/\mathcal{M}_\infty)$. Let us mention the uncertainties in measuring the right shock angle at large distances, the reason being the weakness of the shock at that part of the computational domain. We have always computed this angle with the higher resolution available for the particular model considered in order to reduce this uncertainty. The results appear in Table 2 together with the PSST values. We find that our results disagree with those of PSST, especially for low Mach number models. In all PSST simulations, the

calculated shock angle tends always to be larger than θ_a , in some cases by a factor of 2. A similar result was pointed out by Ruffert & Arnett (1994) in their Newtonian computations, the discrepancies, however, being smaller. We have found also that to be the case for high Mach number flows, where we obtain differences up to roughly a factor of 2 with the predicted values. However, for low Mach number models, the agreement between θ_a and θ_c is quite good. We have plotted our results in Figure 15 together with the analytical expectation. We can clearly see that we get qualitatively the right behavior.

There are other interesting results that can be read from Table 2. Our flow patterns always reach the horizon supersonically as theoretically predicted (see, e.g., Shapiro & Teukolsky 1983) and in agreement with PSST results. This happens for all models, even for those with asymptotic subsonic Mach numbers (ultrarelativistic models UB0 and UC0). Model UC0 is almost in the limit, but its inner boundary is not placed at the horizon but at $r = 2.2M$. All models show their maximum Mach number values at the innermost zone, the upwind values being always larger than the downwind ones (except for model MC1 due to its detached bow shock). The reason for this is that the upwind and downwind velocities have similar values, while the downwind local sound speed is always larger than the

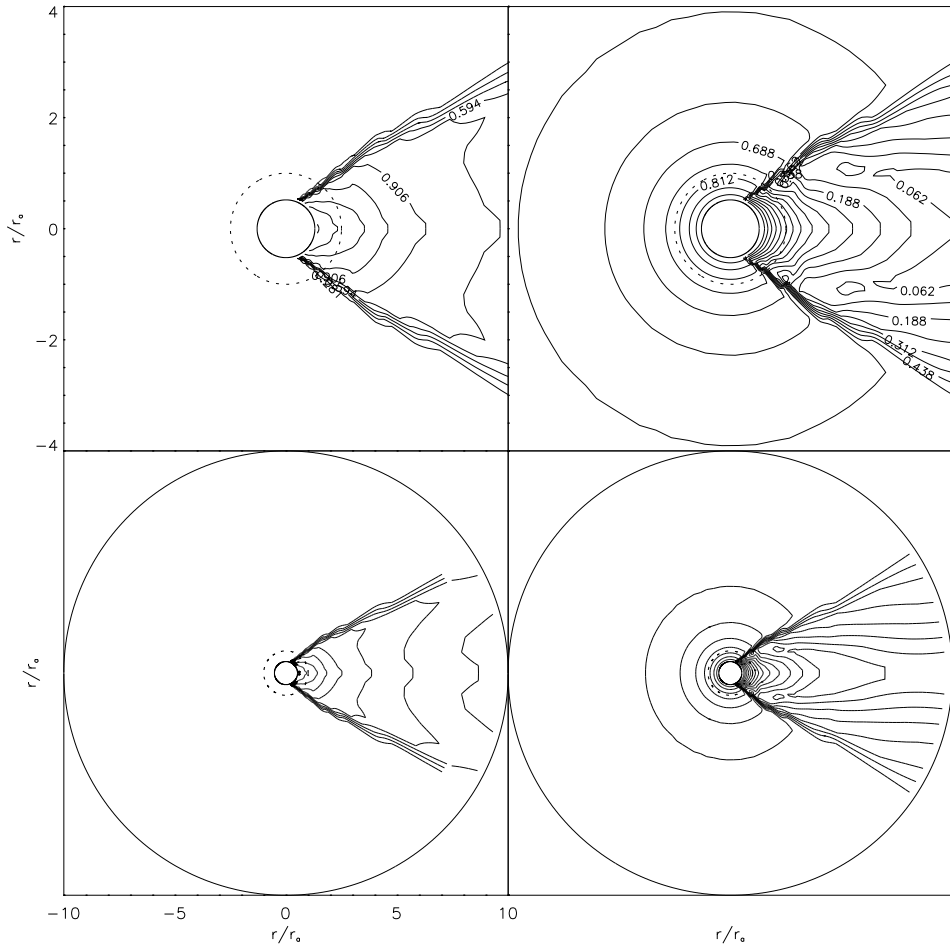


FIG. 7.—Top: Close-up view of the logarithm of density (left) and velocity for model MB2 at $t = 750M$. Bottom: Full computational domain view.

upwind one. This is due to the piling-up of material in the wake of the accretor as the evolution proceeds, which makes the density and pressure to increase considerably there.

We have obtained a very good agreement with analytical one-dimensional estimates by analyzing the flow velocity along the line $\theta = \pi$ in the upwind direction. The flow velocity has to approach the free-fall speed as it gets closer to the horizon:

$$v \approx v_{\text{ff}} = \left(\frac{2GM}{r} \right)^{1/2} \quad (26)$$

assuming that r is much smaller than the *transonic radius* (Shapiro & Teukolsky 1983):

$$r_s = \frac{5 - 3\gamma}{4} \frac{GM}{c_{s\infty}^2} \quad 1 \leq \gamma < \frac{5}{3}. \quad (27)$$

This is a valid assumption for all mildly relativistic models. We have computed equation (26) at r_{\min} for the different models. For the subset of low Mach number mildly relativistic models (MA1, MB1, and MC1), we have $r_{\min} = 3.85M$, which gives, at that distance, $v_{\text{ff}} = 0.72$. This is in perfect agreement with the numerical computed values. For the high Mach number mildly relativistic models (MA2,

MB2, and MC2), we have $r_{\min} = 2.16M$, which gives $v_{\text{ff}} = 0.96$. Again, the agreement is complete. Let us notice that model MC1 is a special case: the presence of the detached bow shock in front of the hole in the upwind direction decelerates the material. This makes it impossible for the fluid to reach the hole at the free-fall speed. In this case, the fluid falls onto the hole at a lesser speed of $0.48c$. The maximum velocity in the downwind direction, at the rear part of the hole, is in this model even larger than at the front part.

A morphological feature common to all models once steady state is reached is the small deviation, in the upwind direction, of the final solution from the spherical one. This can be noticed by looking at the velocity contours of the different models. In the supersonic models, one can see that these lines are totally spherical around the central object, in the upwind domain bounded by the shock cone. In particular, in Figure 2, it is clearly visible how these contours become gradually more spherical as the solution approaches to steady state. This feature is also true for model MC1. Although in this case the shock is detached, the isolines are spherical around the hole.

3.3. Ultrarelativistic Models

Figures 10–14 show the results of our simulations for the subset of ultrarelativistic models of Table 1. As before, we

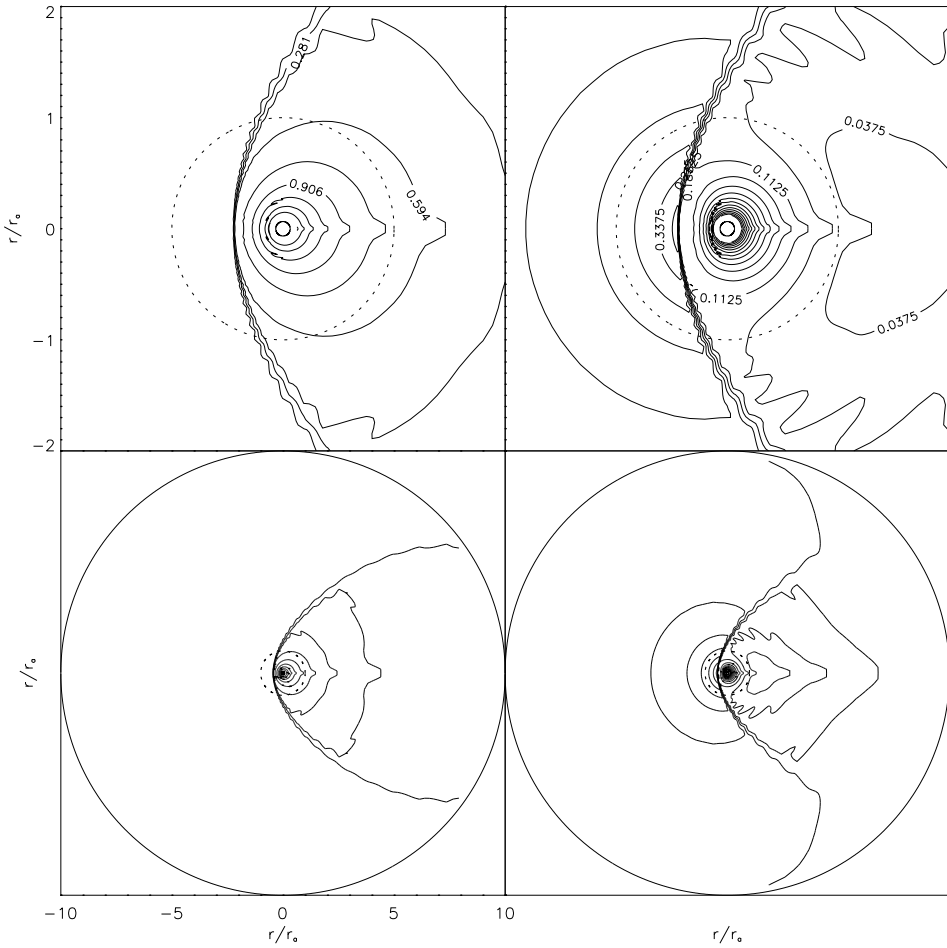


FIG. 8.—*Top:* Close-up view of the logarithm of density (*left*) and velocity for model MC1 at $t = 2000M$. *Bottom:* Full computational domain view. Note the presence of a *detached* bow shock, which is a feature unique to this model.

plot isocontours of the logarithm of the density and velocity in both the whole domain (*bottom panels*) and a smaller region surrounding the hole. As mentioned earlier, these models are ultrarelativistic from the thermodynamical point of view as the initial sound speed is almost as large as its maximum permitted value given by equation (25). In addition, two of these models have a large initial flow velocity (UA2 and UB1) and have not been previously computed. We cannot perform a direct comparison of these figures with those of PSST, as they did not plot them. A comparison can be performed in the computed mass accretion rate only.

The morphology of these ultrarelativistic flows is completely equivalent to what we found previously for mildly relativistic flows. We obtain a completely stable accretion cone attached to the accretor in models UA1, UA2, and UB1, while models UB0 and UC0 do not present shocks as they are subsonic at infinity. These two models present a very small deviation from spherical symmetry at small distances from the hole, as can be seen in the top panels of Figures 10 and 14.

The dynamical timescales at which these models reach the final stationary state is much smaller than in the previous mildly relativistic models. All of them show stable configurations and constant mass accretion rates after

about $50M$ (see below).

We have also computed the shock opening angles for models UA1, UA2, and UB1. Again, we find good qualitative agreement with the predicted values, especially for low Mach number flows (see Table 2 and Fig. 15). The differences are never larger than a factor of 1.3 (the worst case is model UA2). However, we get half the value of PSST for model UA1, the only one we can compare, which they clearly overestimated.

It is remarkable the stability of the position of the stagnation point in the ultrarelativistic models compared with the mildly relativistic ones. This is particularly true for our two subsonic models, UB0 and UC0, for which after $20M$ its value no longer changes in time, as can be seen in Figure 16c. The comparison between mildly and ultrarelativistic models with the same γ and M_∞ (MA1-UA1, MB1-UB1) reveals that the latter ones always have larger values of r_{sp} . This is not surprising, as their asymptotic velocity is always larger.

In Table 2 we see that the maximum upwind velocities are always larger than 0.9 and in some cases reaches well into the ultrarelativistic regime. This is the case of models UA2 and UB1, which reach values larger than 0.99 (note that the initial velocities of these two models are already quite large). Notice that here we can not apply equation (26)

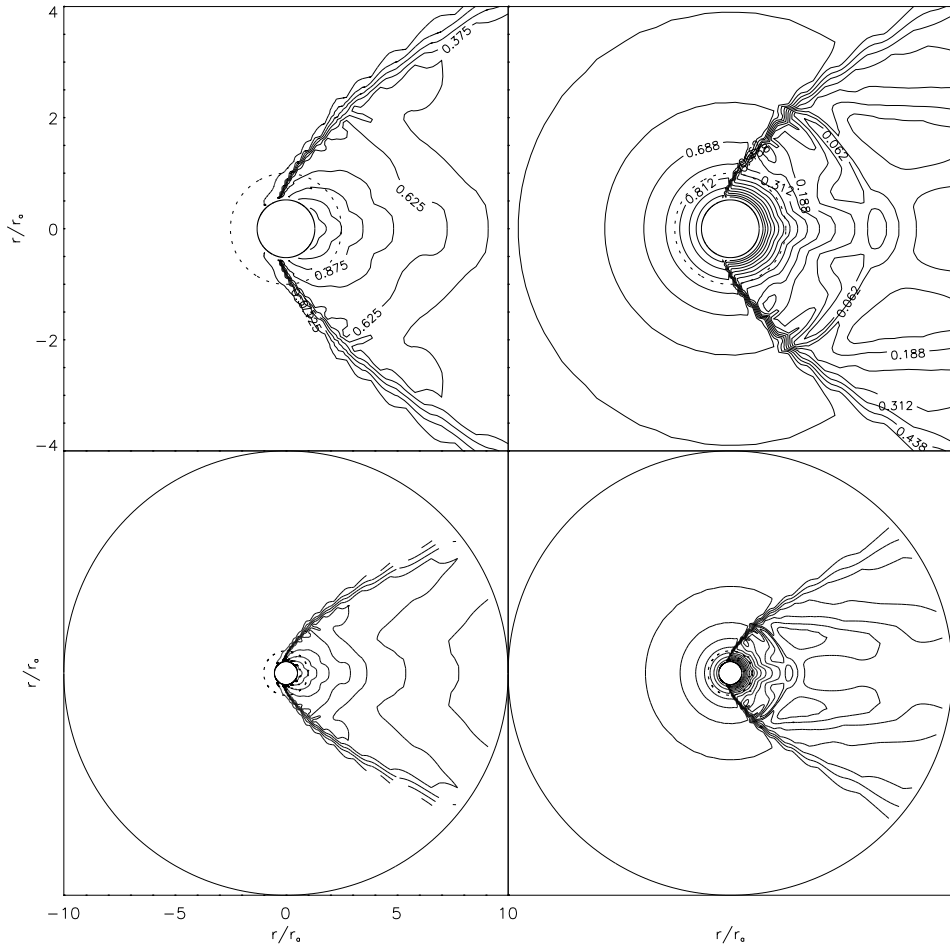


FIG. 9.—*Top*: Close-up view of the logarithm of density (left) and velocity for model MC2 at $t = 750M$. *Bottom*: Full computational domain view.

to compare the one-dimensional free-fall velocity with our predicted numerical values as the sonic radius is similar to r_{\min} and, in some cases, even smaller.

3.4. Accretion Rates

We can define a *gauge-invariant* mass by considering the volume integral of the relativistic density in a given proper volume as

$$m = \int_V \sqrt{\gamma} D dV . \quad (28)$$

Then, using the continuity equation and making use of Gauss theorem, one can compute the time evolution of the mass as a surface integral over some spherical surface surrounding the hole. In the Schwarzschild geometry the mass accretion rate then reads

$$\dot{m} = -2\pi \int D v^r r^2 \sin \theta d\theta . \quad (29)$$

At the steady state, this quantity should be independent of the radial distance at which it is evaluated. Therefore, it is a perfect indicator to see if the numerical solution has relaxed or not to a steady state configuration. The results of our

numerical simulations are plotted in Figures 17a, 17b, and 17c, which display the normalized mass accretion rates for our subsets of low Mach number mildly relativistic models, high Mach number mildly relativistic models, and ultrarelativistic models, respectively. In addition, Table 3 summarizes our mass rate computations and shows a

TABLE 3

MASS ACCRETION RATES

| Model | $t_{\max}(M)$ | $\dot{m}/\dot{m}_{\text{can}}$ | $\bar{\dot{m}}/\dot{m}_{\text{can}}$ | PSST Results |
|-----------|---------------|--------------------------------|--------------------------------------|--------------|
| MA1 | 4000 | 2.1 | 1.8 | 5.0 |
| MB1 | 4000 | 2.4 | 2.1 | 6.1 |
| MC1 | 2000 | 4.5 | 3.7 | 6.4 |
| MA2 | 750 | 4.1 | 3.9 | 1.5 |
| MB2 | 750 | 4.3 | 4.2 | 2.6 |
| MC2 | 750 | 10.0 | 10.2 | 5.2 |
| UA1 | 200 | 3.7 | 3.3 | 9.9 |
| UA2 | 120 | 25.0 | 24.1 | ... |
| UB0 | 200 | 4.6 | 4.6 | 6.7 |
| UB1 | 200 | 27.0 | 26.8 | ... |
| UC0 | 200 | 21.0 | 21.0 | 4.9 |

NOTE.— t_{\max} is the time maximum time of the simulation, $\dot{m}/\dot{m}_{\text{can}}$ is the scaled value of the mass accretion rate at the end of the simulation, and $\bar{\dot{m}}/\dot{m}_{\text{can}}$ is the mean value of the normalized mass accretion rate. Last column shows PSST results.

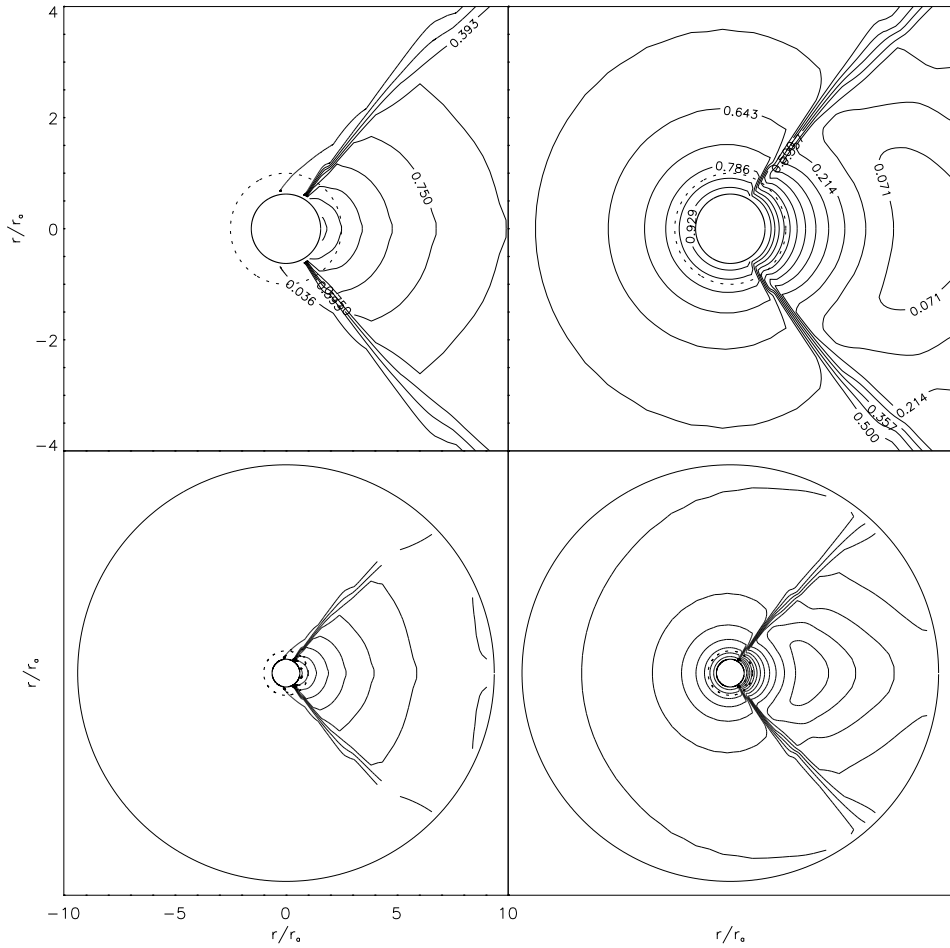


FIG. 10.—*Top*: Close-up view of the logarithm of density (*left*) and velocity for model UA1 at $t = 200M$. *Bottom*: Full computational domain view.

comparison with previous results. The rates have been always normalized to the canonical value proposed by PSST:

$$\dot{m}_{\text{can}} = \frac{4\pi\lambda M^2 \rho_\infty}{(v_\infty^2 + c_{s\infty}^2)^{3/2}}, \quad (30)$$

where M is the mass of the hole and λ is a dimensionless parameter given by (Shapiro & Teukolsky 1983):

$$\lambda = \left(\frac{1}{2}\right)^{(\gamma+1)/[2(\gamma-1)]} \left(\frac{5-3\gamma}{4}\right)^{(5-3\gamma)/[2(\gamma-1)]}. \quad (31)$$

In practice we have computed equation (29) at two different locations depending on the model considered. For the mildly relativistic models we have always considered a surface defined by the accretion radius. However, this was not always possible for the ultrarelativistic models as, in some cases, it was smaller than r_{\min} as in models UA2, UB1, and UC0. Therefore, we decided to measure the mass accretion rate for all ultrarelativistic models at $r = 5M$.

The main conclusion that emerges from Figures 17a–17c is that all models considered in this work settled down to a final steady state accretion pattern. No evidence for any kind of instability (e.g., flip-flop) is present. All models show a remarkable stable accretion rate during the evolution.

Only model MB2 presents small amplitude oscillations in its way toward the final steady state configuration. Notice that all models have been evolved long enough to account for possible late time wake instabilities that could have affected the accretion rate. From these figures one can see that the subset of ultrarelativistic models shows the fastest transition to steady state, which can be considered accomplished around $50M$ – $100M$. On the other hand, the subset of mildly relativistic models shows a quite slower transition, and, among them, the low Mach number models are the slowest. For this reason the complete evolution of these models demands a lot of CPU time.

From Table 3 one can see that in PSST results, for a fixed value of \mathcal{M}_∞ , the normalized mass accretion rate increases as γ increases from 1.1 to 5/3. We obtain the same kind of behavior for all models. However, the numbers disagree. For the mildly relativistic models we obtain systematically smaller values for low Mach number values ($\mathcal{M}_\infty = 1.5$) and bigger values for high Mach numbers ($\mathcal{M}_\infty = 5$). In the ultrarelativistic regime we cannot compare values as they do not present enough results. On the other hand, we find that for a fixed value of γ all models show that the mass accretion rate grows as \mathcal{M}_∞ increases, the ratio being roughly 2 for the three values of γ considered. This is in disagreement with PSST computations, where they found

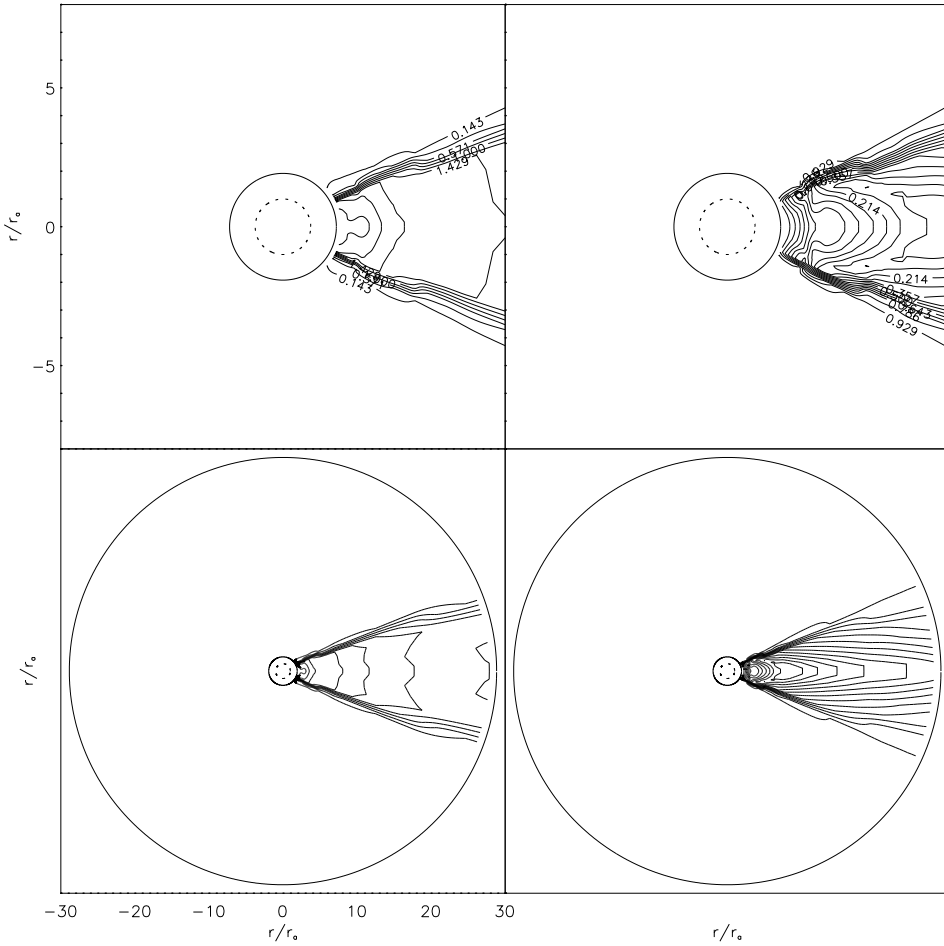


FIG. 11.—*Top:* Close-up view of the logarithm of density (*left*) and velocity for model UA2 at $t = 110$. *Bottom:* Full computational domain view. Note the deceleration of the flow at the shock. The asymptotic velocity of this model is 0.93. The dashed circle, which shows the position of the accretion radius, lies in this model inside the horizon.

precisely the opposite trend, although it is not too clear for large values of γ . Our result is also in contrast with previous calculations in the Newtonian regime (e.g., Ruffert 1994b), where the maximum value of the mass accretion rate corresponds to spherical accretion ($\mathcal{M}_\infty = 0$). Let us notice, however, that this was not either the case in the Newtonian simulations of PSST with $c_{s_\infty} = 10^{-3}$. Their results, both with $c_{s_\infty} = 10^{-3}$ and 0.1, show a peculiar maximum value of $\dot{M}/\dot{M}_{\text{can}}$ for $\mathcal{M}_\infty = 1.5$ independently of the value of γ .

We also obtain that, for a fixed value of γ and \mathcal{M}_∞ , the mass accretion rate increases as the sound speed gets closer to its maximum permitted value (compare models MA1-UA1 and models MB1-UB1). In general, the computed mass accretion rates for the ultrarelativistic models have the largest values.

4. CONCLUSIONS

We have performed a detailed comparative study, over a wide range of initial parameters, of the morphology and dynamics of the relativistic Bondi-Hoyle nonspherical accretion onto a moving Schwarzschild black hole. We have used a high-resolution shock-capturing scheme that employs a linearized Riemann solver as the basic tool for the correct modeling of shock waves. The high performance

of our numerical technique allows for treating the shocks with a high resolution and, consequently, leads to a great accuracy in the morphology and dynamics of the accreting gas. We have found that, in our axisymmetric computations, the accretion flow always proceeds in a steady state fashion showing no signs of instabilities that could have modified in some manner the dynamical accretion rates. We have tested the convergence properties of our scheme by running some models with increasingly higher angular resolutions. In none of the runs the instabilities arose, even with the finer grids.

Generally speaking, our results are qualitatively similar to previous relativistic calculations. The broad flow morphology can be considered identical to that found in PSST calculations, despite the different numerical techniques employed. However, this can be the only reason to explain the important quantitative differences found in some indicators such as the shock opening angles, positions of the stagnation point, or, very specifically, the mass accretion rates.

We have been able to simulate flows well inside the ultrarelativistic regime. Some models of our sample have very high initial asymptotic velocities and, at the same time, asymptotic sound speeds very close to its maximum permitted value.

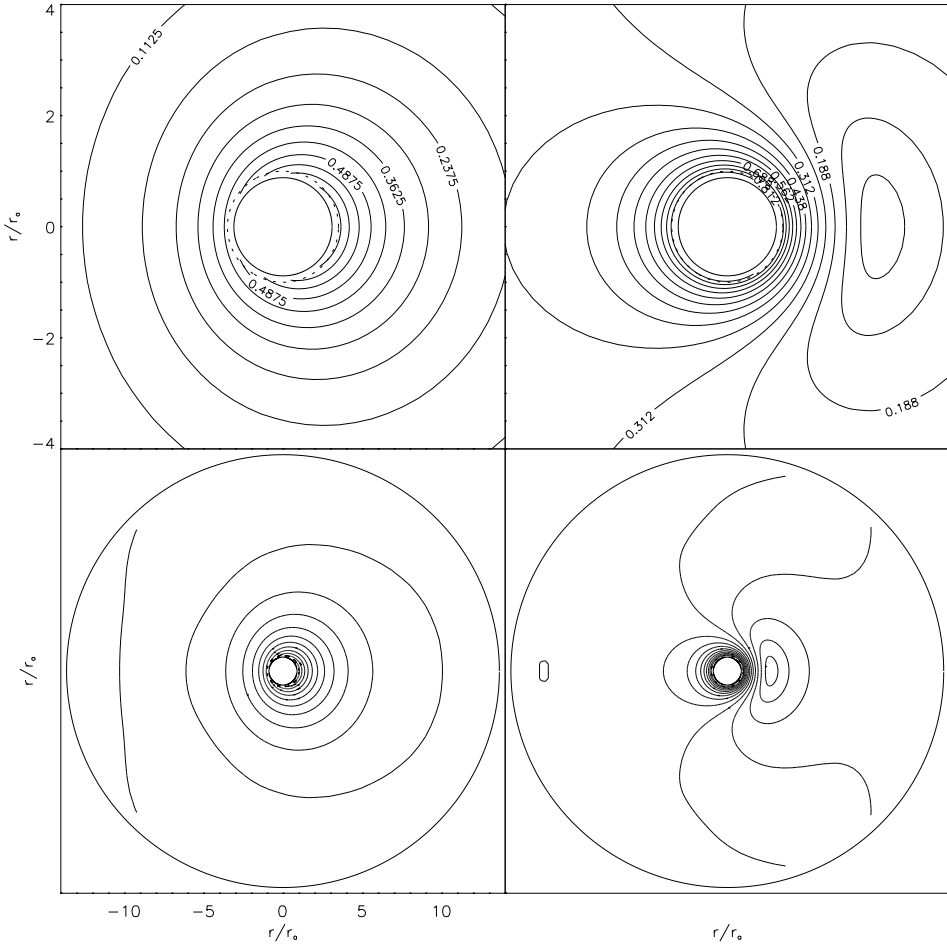


FIG. 12.—*Top*: Close-up view of the logarithm of density (*left*) and velocity for model UBO at $t = 200M$. *Bottom*: Full computational domain view. This is a subsonic model, and hence no shocks are present. Note in the top plot the small deviation from spherical symmetry near the Schwarzschild radius. The position of the stagnation point is very well defined.

The results presented in this paper, as well as the comparisons performed, have served to calibrate the code as a first and necessary step to extend the computations to more complicated configurations. In this sense this paper has to be considered as the first of a series. As the next step, we plan to perform the evolution of the same sample of models in an axisymmetric Kerr background. The code will not need any important modification for this purpose as it is already, in its current version, written in Boyer-Lindquist coordinates for a Kerr spacetime. The results presented here have been obtained by setting to zero the Kerr angular momentum per unit mass parameter. In the long term we plan to extend the code to more general two-dimensional nonaxisymmetric and three-dimensional configurations and perform the same set of simulations. This will permit us to search for the appearance of instabilities that could have been damped in the present axisymmetric computations. It will also allow for the study of more realistic configurations where transverse gradients of velocity and density can be

imposed at the outer boundary to simulate mass transfer in a binary system scenario.

We are also currently working in the more ambitious project of coupling the existing hydro code to an axisymmetric code that solves the Einstein field equations, in the framework of the ADM formalism, for distorted, rotating black hole configurations developed by Brandt & Seidel (1995a, 1995b). Preliminary results can be found in Brandt & Font (1997). The results presented here will serve as an excellent database to compare with our future fully relativistic approach.

We would like to thank Ed Seidel for carefully reading and improving the manuscript. We also acknowledge the suggestions and comments of an anonymous referee. This work has been financially supported by the Max-Planck-Gesellschaft and the Spanish DGICYT (grant PB 94-0973). All calculations have been performed at the AEI in Potsdam.

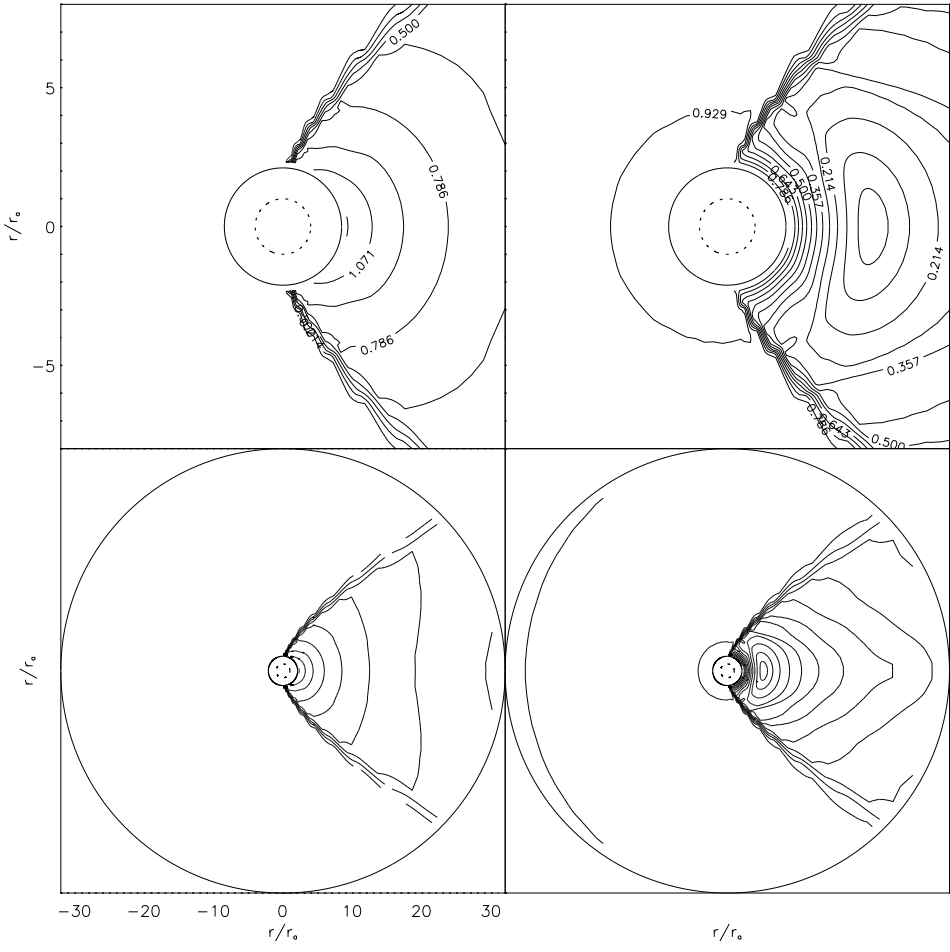


FIG. 13.—*Top*: Close-up view of the logarithm of density (*left*) and velocity for model UB1 at $t = 200M$. *Bottom*: Full computational domain view.

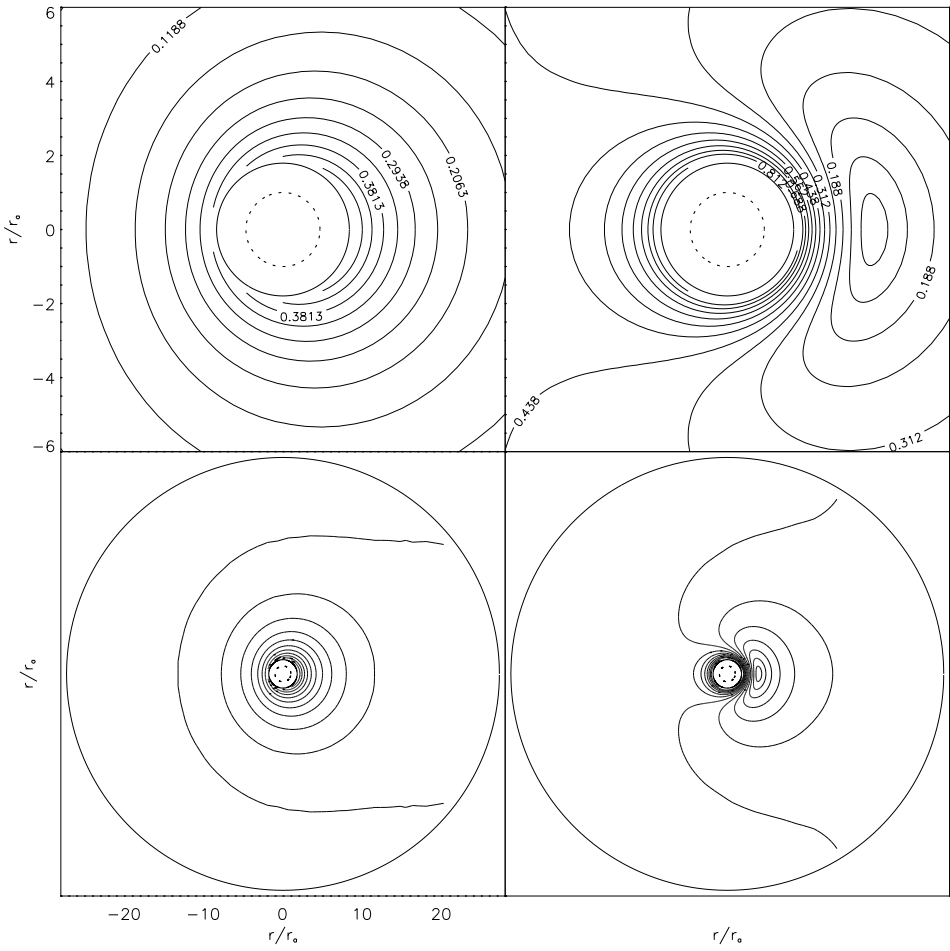


FIG. 14.—*Top:* Close-up view of the logarithm of density (*left*) and velocity for model UC0 at $t = 200M$. *Bottom:* Full computational domain view. As in model UB0 no shocks are present as the asymptotic Mach number is less than 1, and the innermost contours are slightly deviated from spherical symmetry.

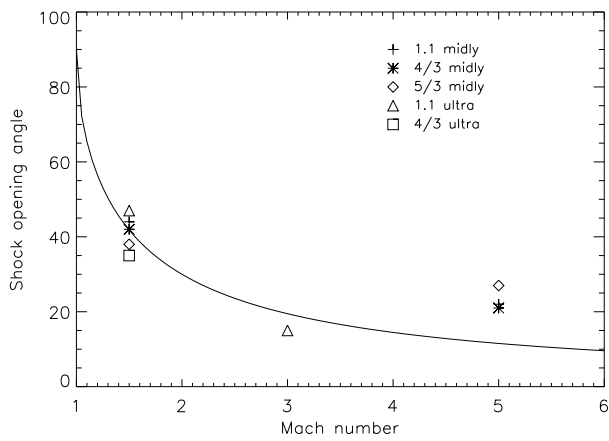


FIG. 15.—Shock opening angle vs. asymptotic flow Mach number. The solid line represents the analytic values at large distances from the hole as given by $\sin^{-1} 1/M_\infty$. The symbols indicate the numerical estimations for the different models and are explained at the top right-hand corner of the plot. The numerical values present the right behavior, and this agreement is better for low Mach number models.

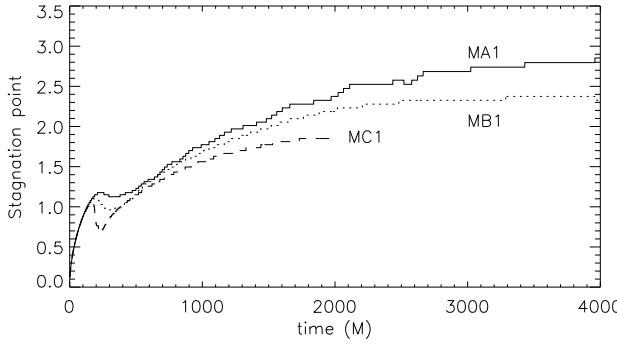


FIG. 16a

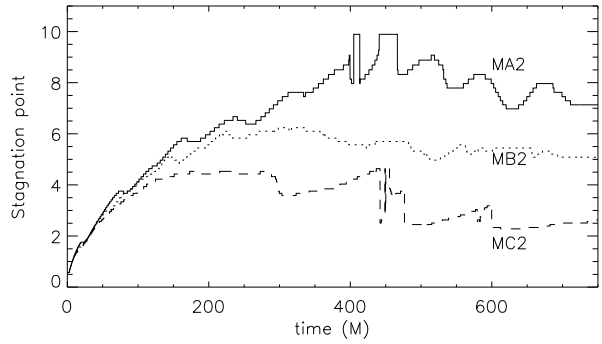


FIG. 16b

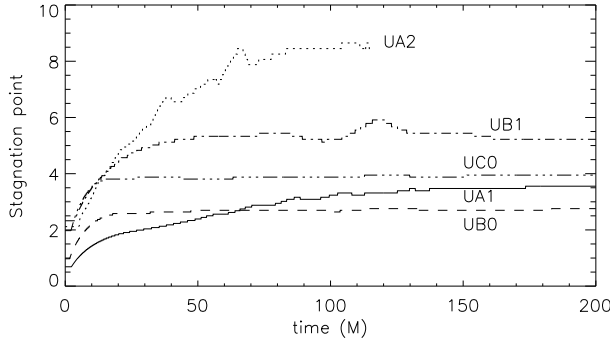


FIG. 16c

FIG. 16.—(a) Evolution of the stagnation point for low Mach number mildly relativistic models (MA1, MB1, and MC1). All of them approach monotonically to a stable fixed position. (b) Evolution of the stagnation point for high Mach number mildly relativistic models (MA2, MB2, and MC2). They present a more unstable transition to a fixed position, if any, than their low Mach number counterparts. Let us mention that with higher angular resolutions (80 and 160 zones; not shown), the transition is much smoother. (c) Evolution of the stagnation point for the ultrarelativistic models (UA1, UA2, UB0, UB1, and UC0). All of them show a remarkable constant value, specially the two asymptotically subsonic models UBO and UC0.

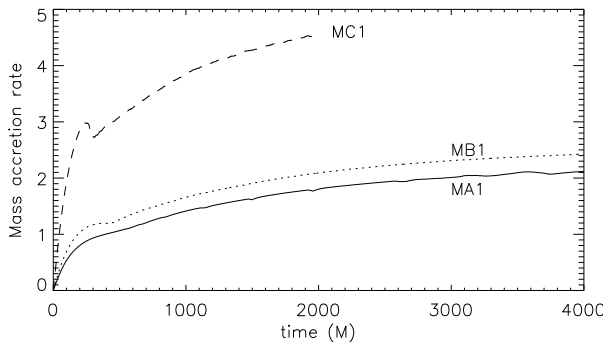


FIG. 17a

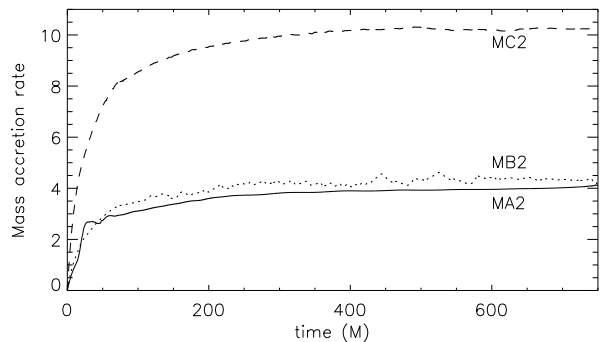


FIG. 17b

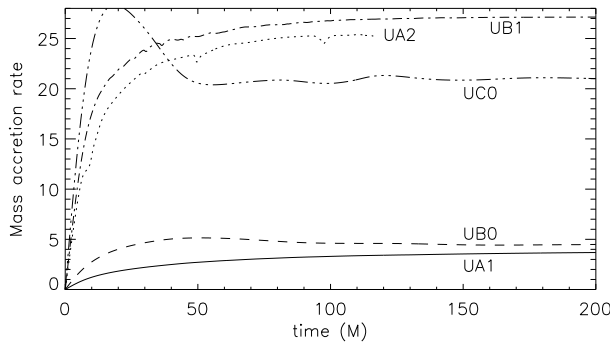


FIG. 17c

FIG. 17.—(a) Normalized mass accretion rate evolution for low Mach number mildly relativistic models (MA1, MB1, and MC1). All models approach steady state, but in a remarkable long amount of time. (b) Normalized mass accretion rate evolution for high Mach number mildly relativistic models (MA2, MB2, and MC2). All models approach steady state in a much shorter timescale than their low Mach number counterparts. Note the tiny oscillations present on model MB1. (c) Normalized mass accretion rate evolution for the ultrarelativistic models (UA1, UA2, UB0, UB1, and UC0). These models show the fastest transition to steady state, quite independently of their initial values of γ and M_∞ .

REFERENCES

- Anzer, U., Borner, G., & Monaghan, J. J. 1987, A&A, 176, 235
 Banyuls, F., Font, J. A., Ibáñez, J. M^a., Martí, J. M^a., & Miralles, J. A. 1997,
 ApJ, 476, 221
 Benesohn, J. S., Lamb, D. Q., & Taam, R. E. 1997, ApJ, 478, 723
 Bondi, H., & Hoyle, F. 1944, MNRAS, 104, 273
 Brandt, S., & Font, J. A. 1997, in Proc. 8th Marcel Grossmann Meeting
 (Singapore: World Scientific), in press
 Brandt, S., & Seidel, E., 1995a, Phys. Rev. D52, 856
 _____, 1995b, Phys. Rev. D52, 870
 Font, J. A., Ibáñez, J. M^a., Marquina, A., & Martí, J. M^a. 1994, A&A, 282,
 304
 Fryxell, B. A., & Taam, R. E. 1988, ApJ, 335, 862
 Hoyle, F., & Lyttleton, R. A. 1939, Proc. Cambridge Philos. Soc., 35, 405
 Hunt, R. 1971, MNRAS, 154, 141
 _____, 1979, MNRAS, 188, 83
 Martí, J. M^a., & Müller, E. 1996, J. Comput. Phys., 123, 1
 Matsuda, T., Inoue, M., & Sawada, K. 1987, MNRAS, 226, 785
 Matsuda, T., Ishii, T., Sekino, N., Sawada, K., Shima, E., Livio, M., &
 Anzer, U. 1992, MNRAS, 255, 183
 Matsuda, T., Sekino, N., Sawada, K., Shima, E., Livio, M., Anzer, U., &
 Börner, G. 1991, A&A, 248, 301
 Norman, M. L., & Winkler, K.-H. A. 1986, in Astrophysical Radiation
 Hydrodynamics, ed. M. L. Norman & K-H. A. Winkler (Dordrecht:
 Reidel), 449
 Petrich, L. I., Shapiro, S. L., Stark, R. F., & Teukolsky, S. A. 1989, ApJ, 336,
 313 (PSST)
 Roe, P. L. 1981, J. Comput. Phys., 43, 357
 Ruffert, M. 1994a, ApJ, 427, 342
 _____, 1994b, A&AS, 106, 505
 _____, 1995, A&AS, 113, 133
 _____, 1996, A&A, 311, 817
 _____, 1997, A&A, 317, 793
 Ruffert, M., & Arnett, D. 1994, ApJ, 427, 351
 Sawada, K., Matsuda, T., Anzer, U., Börner, G., & Livio, M. 1989, A&A,
 231, 263
 Shapiro, S. L., & Teukolsky, S. A. 1983, Black Holes, White Dwarfs and
 Neutron Stars (New York: John Wiley)
 Shima, E., Matsuda, T., Takeda, H., & Sawada, K. 1985, MNRAS, 217, 367
 Shu, C., & Osher, S. 1988, J. Comput. Phys., 77, 439
 Taam, R. E., & Fryxell, B. A. 1989, ApJ, 339, 297
 Taam, R. E., Fu, A., & Fryxell, B. A. 1991, ApJ, 371, 696
 van Leer, B. 1979, J. Comput. Phys., 32, 101
 York, J. W., Jr. 1983, in Gravitational Radiation, ed. N. Deruelle &
 T. Piran (Amsterdam: North-Holland), 175